Nanoscale

PAPER

Cite this: *Nanoscale*, 2016, **8**, 1642

The electronic and transport properties of two-dimensional conjugated polymer networks including disorder†

Jean-Joseph Adjizian,*‡ Aurélien Lherbier,‡ Simon M.-M. Dubois, Andrés Rafael Botello-Méndez and Jean-Christophe Charlier

Received 2nd October 2015,
Accepted 1st December 2015

DOI: 10.1039/c5nr06825h

www.rsc.org/nanoscale

Two-dimensional (2D) conjugated polymers exhibit electronic structures analogous to that of graphene with the peculiarity of π–π^* bands which are fully symmetric and isolated. In the present letter, the suitability of these materials for electronic applications is analyzed and discussed. In particular, realistic 2D conjugated polymer networks with a structural disorder such as monomer vacancies are investigated. Indeed, during bottom-up synthesis, these irregularities are unavoidable and their impact on the electronic properties is investigated using both *ab initio* and tight-binding techniques. The tight-binding model is combined with a real space Kubo–Greenwood approach for the prediction of transport characteristics for monomer vacancy concentrations ranging from 0.5% to 2%. As expected, long mean free paths and high mobilities are predicted for low defect densities. At low temperatures and for high defect densities, strong localization phenomena originating from quantum interferences of multiple scattering paths are observed in the close vicinity of the Dirac energy region while the absence of localization effects is predicted away from this region suggesting a sharp mobility transition. These predictions show that 2D conjugated polymer networks are good candidates to pave the way for the ultimate scaling and performances of future molecular nanoelectronic devices.

Introduction

The electronic structure of graphene exhibits no band gap at the Fermi level but rather a linear dispersion at the *K*-points of the Brillouin zone. The latter means that low energy carriers behave like free relativistic massless particles as described by the Dirac equation.[1,2] This particular electronic structure is a direct consequence of the underlying hexagonal lattice composed of two symmetrically equivalent triangular sub-lattices.[3] The outstanding properties of graphene resulting from its exotic Dirac carriers have produced a large interest, and important efforts have been focused on tuning these properties. Among others, a popular approach to modify the electronic structure of graphene Dirac carriers, and in particular to open a band gap, has been through confinement in so-called graphene nanoribbons (GNRs). In this direction, a breakthrough has come from the bottom-up synthesis of GNRs from the self-assembly of organic precursors.[4] Such an approach yields GNRs with well defined edges and well defined widths, thus allowing an *a priori* knowledge of their properties. Similarly, it was recently shown that a careful choice of monomers could result in the bottom-up synthesis of two-dimensional conjugated polymer (2DCP) networks with Dirac cones at or near the Fermi level.[5] These 2DCP networks can be described by the three fold connection of a wide range of short one dimensional (1D) conjugated polymer chains. With the structural similarities between covalent organic frameworks (COFs)[6,7] and 2DCPs, the advanced bottom-up chemistry strategies developed for COFs have been adapted for the synthesis of 2DCPs, thus leading to the first 2DCP synthesis using tris(4-bromophenyl)amine molecules as monomer precursors.[8,9] Given the set of potential 2D architectures, chemical constituents, and functional modifications, 2DCP networks represent an interesting playground to tune the properties of Dirac carriers. In addition, they should be highly flexible and adjustable to a wide range of fundamental and applied problems.[10,11]

In this paper, the electronic and transport properties of 2DCPs are investigated using first-principles techniques and an accurate tight-binding model combined with an efficient real space Kubo–Greenwood transport formalism. The poly(*p*-phenylene) (PPP)-based 2D-C-$(PP_1)_3$ was chosen as a

Université catholique de Louvain, Institute of Condensed Matter and Nanosciences, Chemin des étoiles 8, 1348 Louvain-la-neuve, Belgium.
E-mail: jean.adjizian@uclouvain.be

†Electronic supplementary information (ESI) available. See DOI: 10.1039/c5nr06825h

‡These authors, contributed equally to this work.

This journal is © The Royal Society of Chemistry 2016

representative member of 2DCPs. It displays an electronic structure similar to graphene with massless Dirac-like fermions but on an energy scale almost ten times smaller.[5] Electronic transport in defective graphene has already been experimentally measured and theoretically investigated[12–15] revealing the importance of structural disorder in the transport performances. Because synthesizing 2DCPs with a bottom-up approach will inevitably introduce structural defects, it is important to study how such defects will affect the transport behavior of 2DCPs. In particular, monomer vacancies randomly distributed in the honeycomb lattice of a mesoscopic size 2DCP are considered in the present study. The real-space Kubo–Greenwood transport formalism allows the exploration of all transport regimes, including quantum localization effects beyond the semi-classical approximation in realistic size systems. Rather long mean free paths and high mobilities are predicted for low defect densities, indicating the good potential of 2DCP-based nanoelectronic devices. Interestingly, at high defect densities, strong localization phenomena originating from quantum interferences of multiple scattering paths are observed in the close vicinity of the Dirac energy region while the absence of localization effects is predicted away from this region with a sharp transition between both regions. This suggests an observable mobility edge at low temperature measurement, which is commonly believed to occur only in 3D systems.[16] This theoretical work conveys insights into these new 2D materials and provides motivation for their experimental synthesis and transport measurements.

Results and discussion

Tight binding parameterization

First-principles calculations were conducted to obtain the optimized geometry and electronic spectrum of the PPP-based 2D-C-$(PP_1)_3$. The electronic structure calculations were first carried out using the self-consistent density functional theory (DFT) method implemented in the SIESTA package[17,18] (see the Method section for details).

Fig. 1A (top panel) illustrates the atomic structure of 2D-C-$(PP_1)_3$. As mentioned already, such 2D networks can be obtained by the self-assembly of monomer precursors. A monomer precursor is composed of a connector atom plus three short polymer chains. In the present case, the chain is reduced to one benzene ring for simplicity and the connector is a carbon atom (*i.e.* C-$(PP_1)_3$). The main difference between the studied 2DCP and the experimentally available analogue (2D-N-$(PP_1)_3$)[8,9] is the nature of the connector atoms, which in this case is a nitrogen atom. Carbon connectors have been chosen in this study as they have the peculiarity to result in a Dirac cone directly at the Fermi energy while the nitrogen connectors, first used in synthesis experiments, tend to shift the Fermi level to higher energies. It is anticipated that 2DCPs with various connectors, including carbon connectors, will be synthesized in the near future.

Despite the atomic accuracy of the bottom-up synthesis strategy, faults will ineluctably occur in the self-assembly resulting in structural defects. In this study, monomer vacancies are considered as prototypical structural defects. To get the first insight

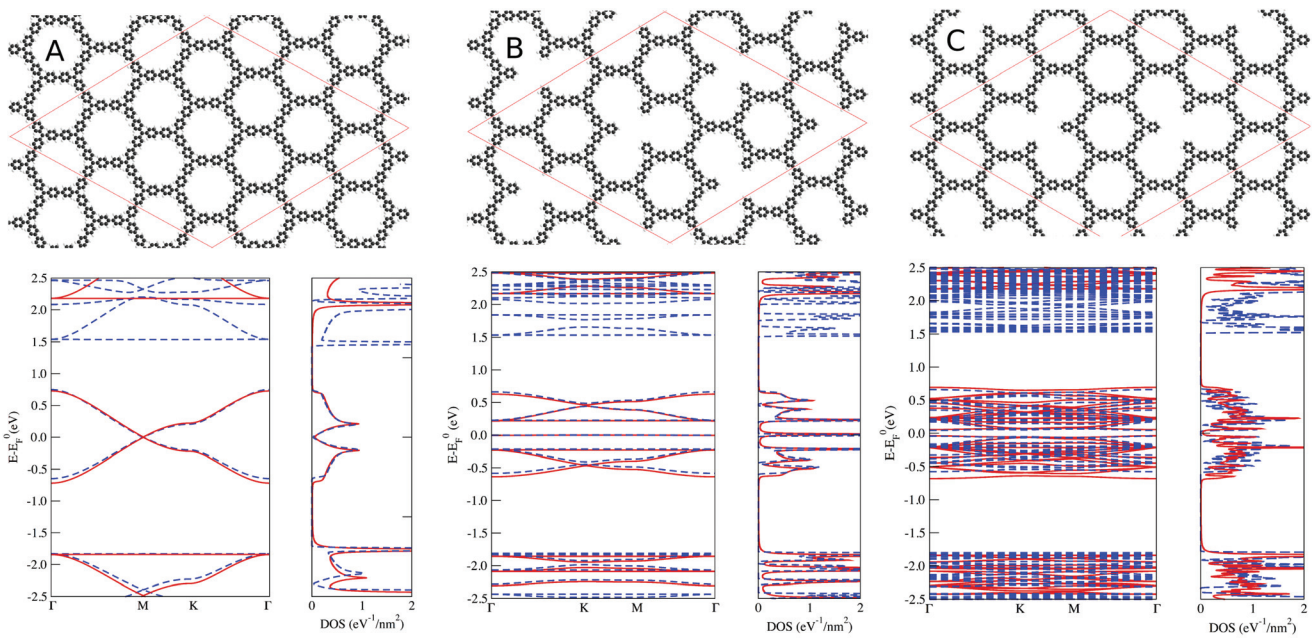

Fig. 1 Top: inside the red cell, 4 × 4 super cells for a pristine 2DCP in (A), containing four monovacancies (12.5%) in (B) and containing two monovacancies (6.25%) with an equivalent number on both sub-lattices in (C). Bottom: *ab initio* (dashed blue line) and tight-binding (red thick line) band structures and densities of states (DOS) of the corresponding atomic structures (A), (B), and (C). The Fermi energy is aligned with E = 0 eV.

into the impact of monomer vacancies on the low-energy electronic structure, small 2D-C-$(PP_1)_3$ super cells containing a few defects were first investigated (see Fig. 1B and C).

The band structures and densities of states (DOS) corresponding to the pristine and defective 2D-C-$(PP_1)_3$ are reported in Fig. 1 (bottom panels). To estimate the percentage of defects, the number of vacancies per cell is calculated. Each monomer vacancy corresponds to a missing monomer precursor. For example, in a pristine 2 × 2 cell, there are eight monomers, if one single-monomer vacancy is created in this cell, the concentration of defects n_v becomes 12.5%. The equilibrium Fermi level ($E_F{}^0$) is taken as the energy reference. Fig. 1 compares the band structures computed from first-principles (dotted blue lines) with results obtained from an adjusted tight-binding (TB) model (red lines). In this orthogonal third nearest neighbors π–π* TB model, the hydrogen atoms are not explicitly accounted for. Instead, the hydrogenated carbon on-site energies are modified to integrate the hydrogen neighbors (as routinely performed for instance in TB models of GNRs). The parameters of the TB model, *i.e.* the on-site terms (ε_{p_z}) and hopping terms ($\gamma(d)$), are summarized in Table 1. Further details are given in the methodology section. As shown in Fig. 1, a very good agreement is achieved for the low-energy spectrum of both the pristine and the defective 2D-C-$(PP_1)_3$ especially in the region close to the Fermi energy. The dispersion relations of the high-energy conduction bands are similarly accurate but the TB approximations come with a shift of these bands to higher energies.

At low energies, the pristine 2DCP presents a band structure and DOS very similar to that of graphene but on a different energy scale (see Fig. 1A). An almost symmetric π–π* band is reported with a linear dispersion in the vicinity of the Fermi energy, forming a Dirac cone. These π–π* bands encompass an energy window of approximately 1.5 eV, that is roughly ten times smaller than in the graphene spectrum. The low energy bands are isolated from the rest of the spectrum (and in particular from the σ bands) by energy gaps of ~1.5–2.0 eV. Plotting the wave-functions for the highest occupied band (see Fig. 1 in the ESI†) reveals that the states are dispersed over the whole 2DCP skeleton which is a typical signature of 2D conjugated polymers. However, these *ab initio* calculations are carried out at 0 K, and at room temperature benzene rings will have the freedom to rotate. In order to understand the effect of such a rotation, dihedral angles have been tuned manually for a given branch or a single benzene ring. Fig. 2 in the ESI† illustrates the four possible situations. For each structure, the electronic band structure was calculated and displayed using a specific path in the Brillouin zone. These results clearly demonstrate that the electronic properties for the π–π* bands are not strongly affected by the rotation of the benzene rings. The only noticeable difference concerns the shift of the Dirac cone which is observed to be slightly delocalized from the high symmetry *K*-point of the Brillouin zone. A similar behavior has previously been observed in graphene in the presence of defects[14] and is due to ground state symmetry breaking. These *ab initio* calculations demonstrate the robustness of the electronic properties and specially the conservation of the Dirac cone at higher temperatures, and further highlight the possible use of these quasi-2D conjugated polymer networks for different nanoelectronic applications.

The band structure of a 2 × 2 super cell containing a single monomer vacancy (*i.e.* a concentration of n_v = 12.5%) is displayed in Fig. 1B. Flat bands associated with defect-induced localized states are reported around the Fermi level. Narrow band gaps are observed on each side of the zero energy mode and the band structure conserves an overall mirror symmetry between valence and conduction bands. From the emergence of a zero energy mode, it is straightforward to anticipate that electronic transport will be mainly affected in an energy window around the Fermi level. However, one has to stress out that the peculiar band structure reported in Fig. 1B results directly from the periodic boundary conditions imposed on the system. In this configuration, vacancies form a regular super-lattice affecting exclusively one of the two triangular monomer sub-lattices of the pristine 2DCP. It has already been demonstrated for graphene that having a local disorder either on only one or on both sub-lattices changes qualitatively the low energy spectrum.[12,19,20] To understand if a similar behavior is observed in 2DCP, larger super-cells have been considered where the monomer vacancies impact both sub-lattices. Such a case of a 4 × 4 super-cell containing one monomer vacancy on each sub-lattice (n_v = 6.25%) is illustrated in Fig. 1C. The emergence of defect induced flat bands in the low energy spectrum appears clearly in the DOS and the mirror symmetry between valence and conduction bands is maintained. However, one notes the absence of a central peak and notes instead the presence of a unique small gap. Further consideration of different vacancy arrangements while still preserving the balance in the sub-lattice disorder (see Fig. 3 in the ESI†) emphasizes the dependence of the low energy spectrum upon the detailed arrangement of defects within a periodic cell. Conclusions can be drawn from these preliminary calculations of periodic arrangements of vacancies: (i) there is no zero mode observed in the case of compensated sub-lattices as compared to the fully uncompensated case reported in Fig. 1B, (ii) the width of the so-induced energy gaps depends on the detailed atomic configuration. An enlightening discussion on the emergence/absence of zero energy modes in honeycomb lattices can be found in ref. 12.

Table 1 Tight-binding parameters of the pristine 2DCP. Two carbon species are accounted for in this model, depending on whether they are hydrogenated edge atoms (C_2), or not (C_1). The on-site terms (ε) of each carbon species is given first, followed by the hopping terms (γ_0) as defined in the text. All the energy terms are given in eV

	On-site terms (ε)
C_1	0.00
C_2	−0.60
	Hopping terms (γ_0)
C_1–C_1	−3.55
C_1–C_2	−2.85
C_2–C_2	−2.55

 This journal is © The Royal Society of Chemistry 2016

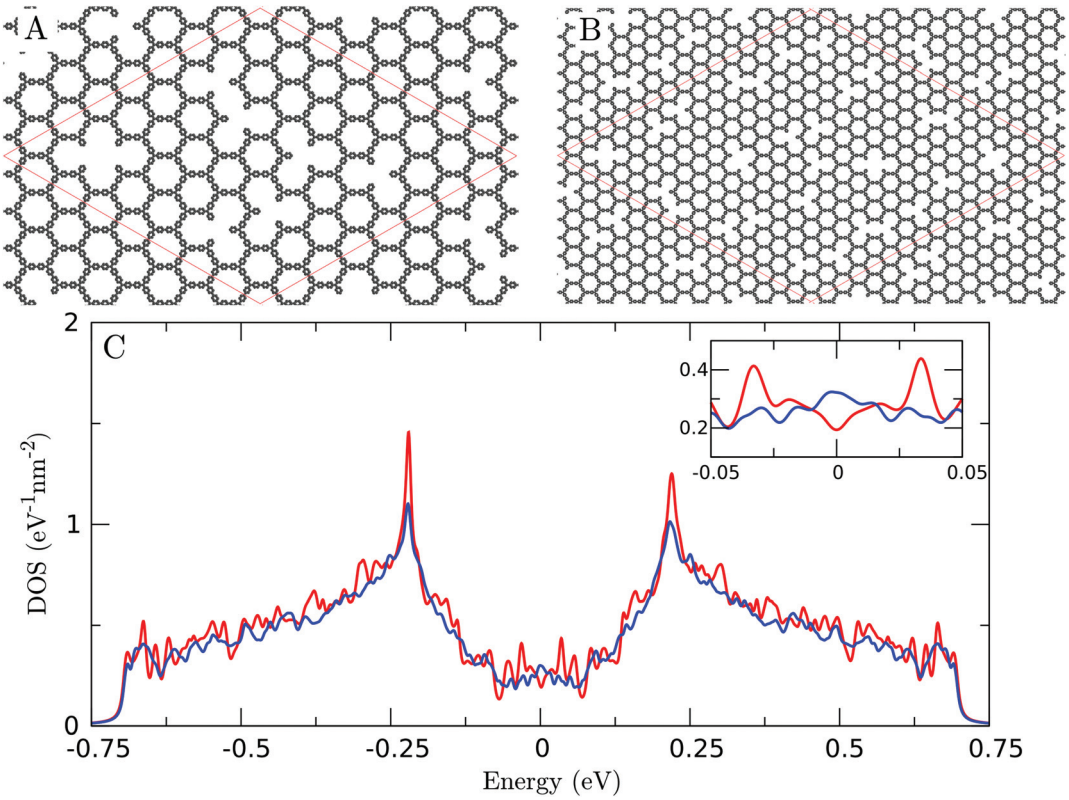

Fig. 2 (A) Atomic structures of defective 2DCP: 8 × 8 (A) and A 16 × 16 (B) super-cell containing 6.25% of vacancies (with the same number of vacancies on each sub-lattice), (C) the respective DOS for A (red) and B (blue) (inset is a zoom in at the Fermi level).

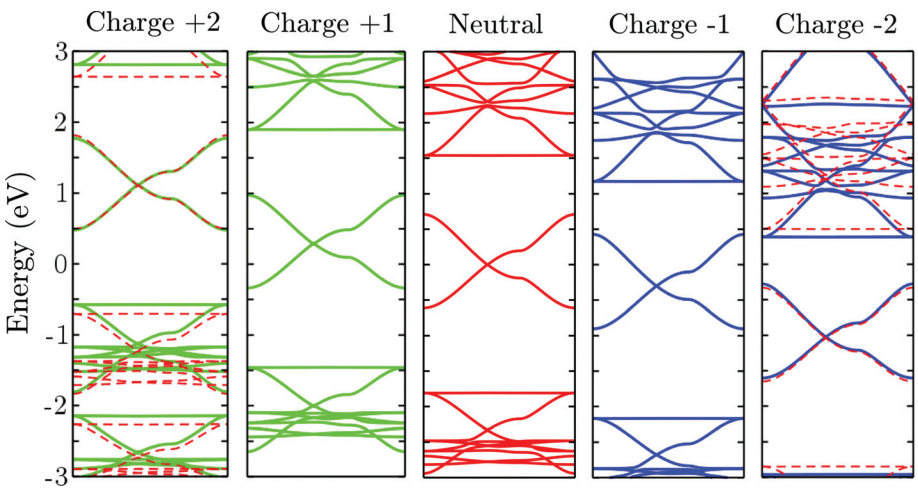

Fig. 3 Electronic band structures using the simulated doping technique coded in SIESTA for a 2D-C-$(PP_1)_3$ primitive unit cell. The Fermi energy is set to zero. The band structures of positively, neutral, and negatively charged systems are plotted with green, red, and blue lines respectively. To evidence the rigid-band approximation, the shifted neutral band structure is also reported in dashed red lines in the case of an excess charge of −2|e| and +2|e|.

Transport properties

Larger disordered super-cells are required to capture the physics of defective mesoscopic 2DCP samples. Fig. 2 depicts the atomic structure and DOS of disordered 8 × 8 and 16 × 16 super-cells containing n_v = 6.25% of defects with compensated sub-lattices. While the 4 × 4 super cell displayed a noisy DOS whose positions of the peaks depend on the actual atomic

structure (Fig. 1C and 3 in the ESI†), these features are progressively averaged out as the system becomes larger as observed already for the 8 × 8 super cell DOS. Eventually, the 16 × 16 super cell exhibits a small hump in the DOS around the Fermi level associated with the overlap of defect-induced localized states whose resonant energy is very close to the Fermi level. Overall, 2DCPs show a similar behavior as graphene upon inclusion of vacancies.[12,15] When vacancies are located on one sub-lattice, the corresponding symmetry is broken, and a gap is observed on both sides of the Fermi level. Zero energy modes are also observed through the sharp peaks at the Fermi energy. When vacancies are randomly distributed, it follows the theorem described in ref. 21, and the gap on each side of the Fermi level disappears and a broader central peak is observed.

Transport properties of this defective 2DCP are then investigated, and it is important to consider the charge and discharge of the system as it would be associated with the application of a gate voltage. The transport approach is based on linear response approximation within the real-space Kubo–Greenwood methodology, where the filling in electrons or holes is accounted for as a rigid shift of the Fermi energy (E_F) with respect to the equilibrium Fermi energy position (E_F^0). As reported in Fig. 3, the rigid shift model provides a very good approximation for the charge/discharge in such conjugated polymer crystals. Fig. 3 shows the impact on the electronic band structure of adding and removing electrons from pristine 2D-C-$(PP_1)_3$. Here, a background charge density has been added to the first-principles calculations in order to preserve overall charge neutrality as is commonly done to simulate doped systems. Bands near the equilibrium Fermi energy (equivalently around the Dirac point) are not significantly modified by variations of the charge density up to two electrons per unit-cell which corresponds to the depletion/filling of an entire electronic band. The integrity of the system is maintained and the 2D-C$(PP_1)_3$ geometry is only slightly modified. The calculations predict a change in the dihedral angle of a maximum of 1.42° of the PPP branches. This stability is generally observed in carbon allotropes where the σ bonds ensure the mechanical stability.[22] Such a large variation of the charge density, $\Delta n = 7.5710^{13}$ cm^{-2}, would correspond to a gate voltage (ΔV_g) of 12.13 V for an associated gate capacitance (C_g) of 1 μF cm^{-2} (that is approximately the gate capacitance of a 15 nm thick HfO_2 film[23]). One can therefore imagine probing entirely the π bands in a transport experiment provided a good dielectric is used for the oxide gate. An alternative to the physical electrostatic gating with an oxide substrate is the electrochemical gating. It consists of putting the system in a charged ionic solution which for 2DCPs is a suitable approach owing to their porous nature.

The transport properties of large 2D-C-$(PP_1)_3$ sheets (400 × 400 nm^2, containing ~2.4 millions of atoms ignoring the hydrogen atoms) with a concentration of vacancy defects (n_v) randomly distributed in the honeycomb lattice ranging from 0.5% to 2.0% are investigated using the just-developed TB model. Since the position of monomer vacancies is random, the sub-lattice disorder is almost compensated (~50% of defects in each sub-lattice with a maximum deviation of 5%). The DOS of these large 2DCPs, displayed in Fig. 4A, are calculated using the Haydock recursion technique[24] using a set of eight random phase wavepackets and are averaged on two disorder configuration samples (note that an important average

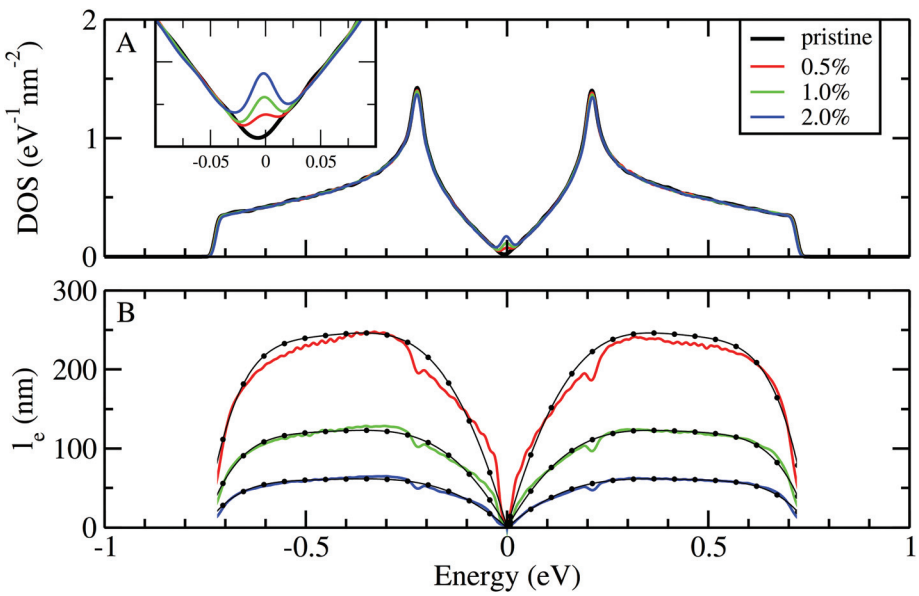

Fig. 4 (A) Densities of states of 400 × 400 nm^2 of a 2D-C-$(PP_1)_3$ in the pristine case and with various concentrations of vacancy defects randomly distributed (0.5%, 1.0%, 2.0%). (B) Carrier mean free paths (l_e) of the corresponding defective 2DCP monolayers. Black dotted lines are fits obtained following the Fermi golden rule.

 This journal is © The Royal Society of Chemistry 2016

over disorder configurations is already obtained within a single sample as the system is very large). As highlighted previously in Fig. 2, when considering a random distribution of vacancy in a large enough 2DCP, the DOS is characterized by a small hump located at the Dirac point.

The time-dependent diffusivity curves $D(E, t)$ computed within the Kubo–Greenwood formalism are the signature of various transport regimes. In a semi-classical picture, the diffusivity increases and then saturates to a maximal value $D^{\max}$ in the thermodynamic limit, *i.e.* after a large enough number of scattering events. However, in the quantum regime, constructive interferences between scattering paths can yield localization which causes a decrease in diffusivity. Eventually, for a long enough propagation time, or equivalently for a long enough propagation length, the diffusivity decreases exponentially and carriers enter the strong localization regime. Fig. 6A and B show the diffusivity of the defective 2DCPs with 0.5% and 2.0% monomer vacancies, respectively, as a function of the propagation time and for an energy range encompassing the π and π* bands. It is obvious from this picture that the diffusivity is strongly reduced in absolute value with an increasing density of vacancy denoting the global degradation of transport properties which are described in more detail in the following section. At first, we report on the elastic mean free path and the semi-classical carrier mobility, *i.e.* l_e and μ_{sc}, that are semi-classical quantities deduced from the maximum of diffusivity curves. Then, the impact of quantum interferences is assessed and localization phenomena are discussed later.

The calculated elastic mean free path (l_e) is plotted in Fig. 4B. The maximum of l_e is reached just after the van Hove singularity ($E \sim \pm 0.3$ eV), and drops rapidly to values close to zero at the Dirac point ($E = 0$ eV) and at the band extrema ($E \sim \pm 0.7$ eV). Even at defect concentrations as high as 2% the elastic mean free path is around 50 nm, and it surpasses 200 nm for 0.5% vacancies. The results associated with the mean free path suggest a tendency to follow the Fermi golden rule and could therefore be evaluated for any concentration as $l_e^{[n_v]} = l_e^{[n_v^0]} \frac{n_v^0}{n_v}$. A good fit for dependence in the energy of $l_e^{[1\%]}$ is given by $l_e^{[1\%]}(E) = A_0 - |\sin(A_1 E)| + A_2 E^2 + A_3 E^4 + A_4 E^6$, with $A_0 = 404.27$, $A_1 = -2.17933$, $A_2 = -1706.07$, $A_3 = 4000.87$, $A_4 = -3972.53$. This fit was used to determine $l_e^{[0.5\%]}$ and $l_e^{[2.0\%]}$ in Fig. 4B (black dotted lines) which confirms the straightforward relationship between defect densities and transport properties.

The charge carriers mobility (μ) can be evaluated as $\mu(E_F, T) = (\sigma(E_F, T))/(en(E_F, T))$, where e is the elementary charge, σ is the conductivity, and $n(E_F, T)$ is the charge carrier density which is defined as

$$n(E_F, T) = \left[\int_{-\infty}^{E_D} \rho(E)\left(1 - f^{FD}(E, E_F, T)\right) dE\right] - \left[\int_{E_D}^{+\infty} \rho(E) f^{FD}(E, E_F, T) dE\right] \quad (1)$$

where $f^{FD}(E, E_F, T)$ is the Fermi–Dirac distribution function for a given Fermi energy E_F and temperature T. $\rho(E)$ is the DOS per unit of area, and $E_D = 0$ eV is the Dirac point energy. The semi-classical mobility (μ_{sc}) is evaluated using the semi-classical conductivity (σ_{sc}) (see the Methods section).

Fig. 5 displays the semi-classical mobility and charge density at room temperature ($T = 300$ K). By definition μ is inversely proportional to n, and the value of the mobility diverges when n tends to zero. Away from this divergence, the semi-classical mobilities are found in the range [2–8] 10^3 cm^2 V^{-1} s^{-1} for concentrations n_v ranging from 2.0 to 0.5%

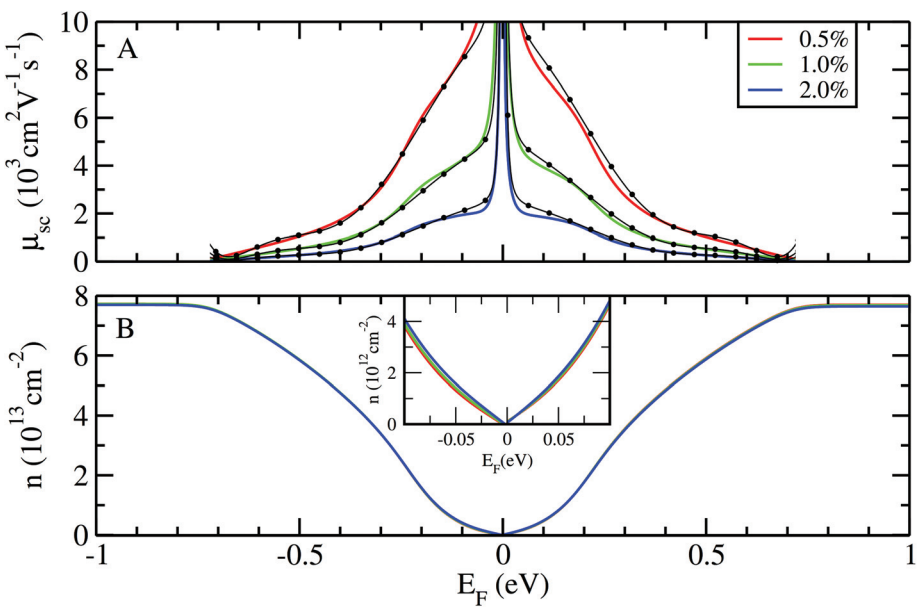

Fig. 5 (A) Charge carrier mobilities (μ_{sc}) and (B) charge carrier densities (n) in the defective 2DCP monolayers as a function of the Fermi energy (E_F).

respectively. Such values of mobilities are high enough to envision electronic devices based on 2DCPs. However, they do not account for other sources of elastic scattering such as charged impurities trapped in the oxide substrate and neither inelastic scattering coming for instance from electron–phonon coupling at a finite temperature, which are beyond the scope of the present paper. As for the mean free path, $\mu_{sc}^{[1\%]}$ can be fitted and used to determine the mobility at any concentration following the Fermi golden rule (black dotted line in Fig. 5A). The fit for the energy dependence of $\mu_{sc}^{[1\%]}$ is given by $\mu_{sc}^{[1\%]}(E) = A_0/E^2 + A_1 + A_2E^2 + A_3E^4 + A_4E^6 + A_5E^8$, with A_0 = 1.09806, A_1 = 4595.83, A_2 = −52860.3, A_3 = 262 905, A_4 = −580 563, A_5 = 462 335. The properties discussed above, *i.e.* l_e and μ_{sc}, are semi-classical quantities that do not account for quantum interferences and carrier localization. From Fig. 6A and B, it seems that time dependent diffusivity saturates at a maximal value indicating a semi-classical regime and the absence of quantum correction. However, on re-scaling the diffusivity to its maximal value and looking closer at the zero energy region (Fig. 6C and D), it turns out that localization effects emerge in the vicinity of the Dirac point. Although these effects are rather small for n_v = 0.5%, the impact of interferences is much clearer for n_v = 2.0%. For n_v = 2.0%, the energy window corresponding to localization is in the range of 50 meV and displays a sharp transition between localized and semi-classical regimes indicating a rapidly varying localization length.

Transport regimes

In order to obtain a deeper understanding of this sharp transition between localized and semi-classical transport regimes, we calculated the inverse participation ratio (IPR) which measures the degree of localization of a wave function. For an ideally localized wave function, *i.e.* localized on a single orbital *j*, IPR is equal to 1. Inversely, the IPR of an ideally delocalized wave function equals $1/N_{orb}$. Fig. 7A shows the IPR for a pristine and a defective 2DCP 16 × 16 super cell. Interestingly, for a pristine 2DCP, the wave function is not fully delocalized (Fig. 7A). This is further highlighted in the ESI Fig. 1B† where the wave function of a pristine 2DCP is calculated for the *K*-point of the Brillouin zone at the Fermi energy. For a concentration of defects of 1.56%, the degree of localization increases

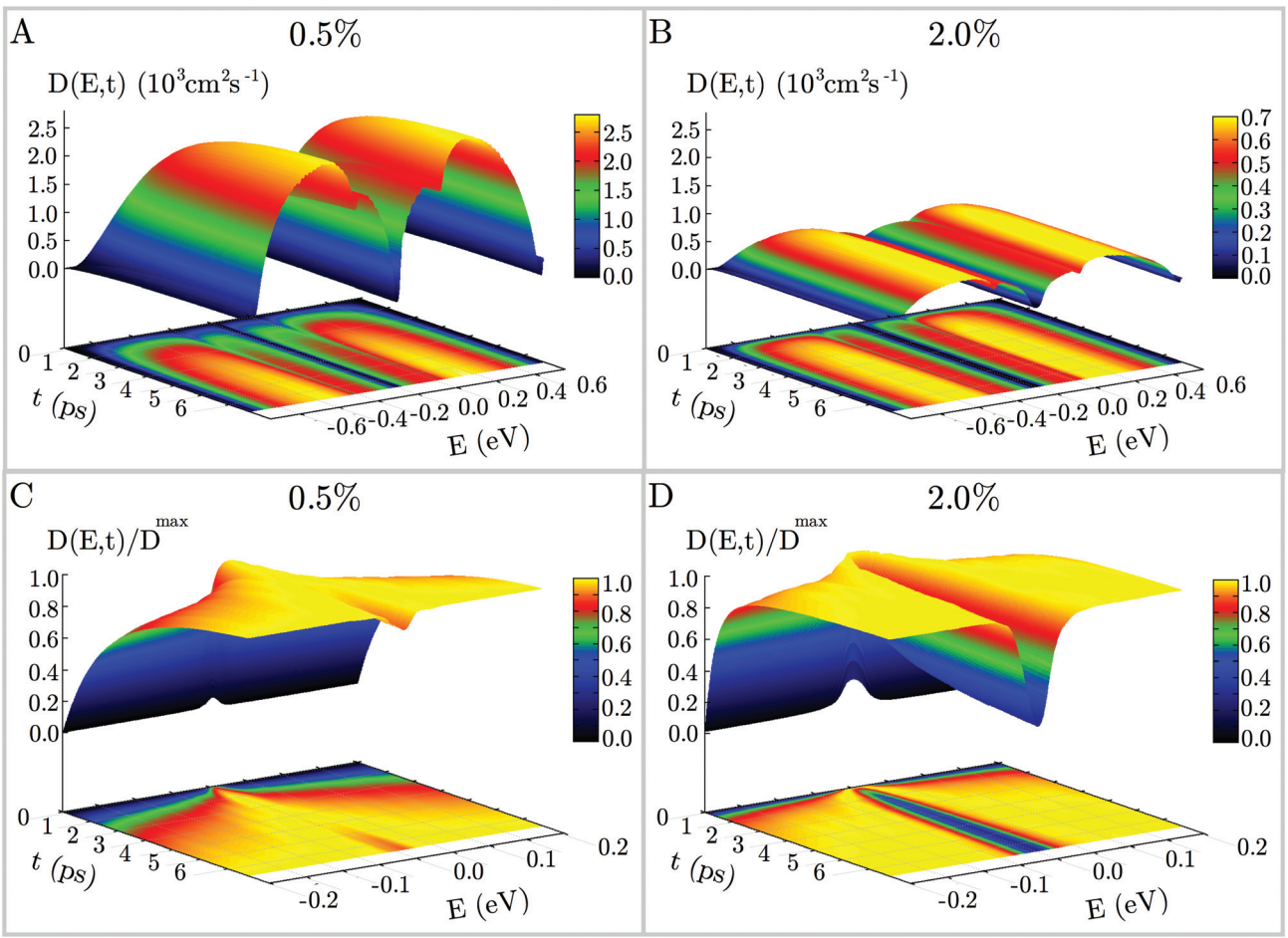

Fig. 6 3D plots of the diffusivity as a function of time and energy for 2D-C-$(PP_1)_3$ with a vacancy defect concentration of 0.5% (A) and 2.0% (B) respectively. (C) and (D) are the normalized diffusivities of (A) and (B) at a smaller energy range.

 This journal is © The Royal Society of Chemistry 2016

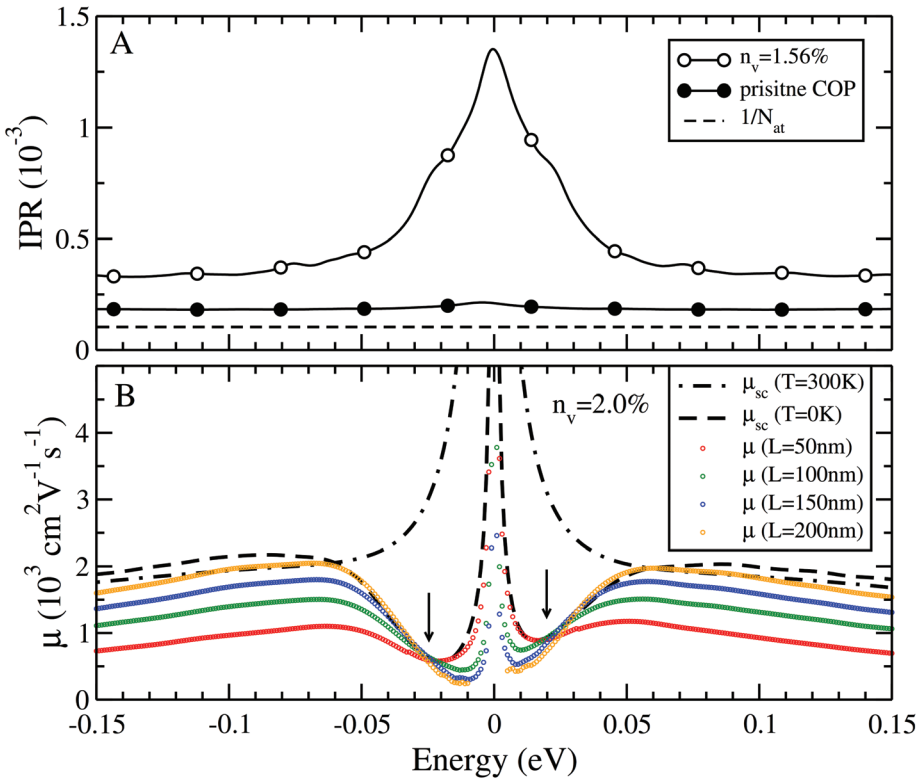

Fig. 7 (A) Inverse participation ratio (IPR) for an ideal delocalized wave function (dashed line), for a pristine (black circle), and for a 1.56% defects (white circle) 2DCP; (B) the mobilities in the semi-classical (μ_{sc}) and in the quantum (μ) regime for a 2DCP containing n_v = 2.0% of randomly distributed vacancies.

as expected and is almost twice the IPR value of the pristine case at energies away from the Fermi level. For energies around the Fermi level, the IPR varies to show an increase in localization with its maximum at E_F = 0 eV. The effects of localization on charge carrier mobility are highlighted in Fig. 7B. One observes that the semi-classical mobility μ_{sc}, see also Fig. 5, strongly varies around the Dirac point as a function of the temperature (black dashed dotted and dashed lines). The quantum mobility (at T = 0 K and accounting for possible quantum interferences) increases as a function of the propagation length and saturates to $\mu_{sc}(T = 0\ \text{K})$ for energies outside the localization window. Around the Dirac point, localization effects are at stake and the quantum mobility vanishes for large enough propagation lengths. These two opposite behaviors create sharp variations in mobility, called mobility edges, around energies indicated by the arrows in Fig. 7B. Fig. 7A and B corroborate the strong localization around the Fermi energy and the two different behaviors leading to the mobility edge in 2DCP. Such a mobility edge is signature of the separation between transport regimes based on extended and localized states and is *a priori* only expected in 3D materials.[16] However, it has been shown that the nature of the disorder plays an important role in this commonly accepted prediction and that the mobility edge can actually be induced in low-dimensional materials.[25,26] This explains why such a mobility edge signature is highly sought in 1D and 2D systems. Similar semimetal–insulator transitions were also reported in graphene.[27,28]

Conclusions

The electronic structures of 2DCPs share various similarities with graphene, notably the linear energy dispersion giving rise to massless Dirac fermion characteristics around the Fermi energy. However, the major differences are the energy bandwidth and the complete isolation of the fully symmetric π–π* bands. This makes the 2D-C-$(PP_1)_3$ an interesting material to probe the transport properties of π–π* manifold. It is predicted that the bottom (top) of the π valence (π* conduction) band could be accessible in a transport experiment using an appropriate high-κ dielectric as the gate oxide. These structures are robust to chemical doping and retain the linear dispersive bands upon large variations of charge density. The transport properties of realistic large 2DCP sheets containing randomly distributed monomer vacancy defects have been investigated. The carriers exhibit good transport properties with long mean free paths and high mobilities (in the range 10^3 cm^2 V^{-1} s^{-1}) allowing one to envision 2DCP-based electronic devices. Sharp variations in the low temperature mobility around the Dirac

point are reported for systems containing large concentrations of defects indicating the possibility of observing a mobility edge in 2DCPs. As the 2DCP topology gives them a flexibility which might not be accessible to graphene, the peculiar electronic and transport properties reported in this study are expected to stimulate further research on these new materials in view of their implementation in future polymer-based electronic devices.

Methods

Ab initio approach

Ab initio calculations have been performed using the SIESTA package.[17,18] The exchange–correlation energy and electron-ion interactions are described using GGA-PBE[29] functional and norm-conserving pseudopotentials[30] in the fully non local form, respectively. A double-ζ polarized basis set of numerical atomic orbitals is used and the energy cutoff for the real-space mesh is set to 300 Ry. A Fermi–Dirac distribution function with an electronic temperature of 10 meV is used to populate the energy levels. The geometries are fully relaxed until the forces on each atom and on the unit cell are less than 0.01 and 0.03 eV Å^{-1}, respectively. Periodic boundaries were applied with an inter-layer vacuum distance >10 Å for single layers. A fine k-point grid of at least 20 × 20 × 1 for monolayers was chosen using the Monkhorst–Pack scheme.[31] Atomic positions and lattice parameters were geometrically optimized prior to band structure calculations. All these parameters ensured the convergence of the ground state properties (geometric and electronic structures) to less than one meV per atom.

Tight-binding model

Tight-binding calculations have been performed using the TB_Sim package. The hopping terms are distant-dependent and read as $\gamma(d) = \pm\gamma_0 e^{-3.37\left(\frac{d}{d_{CC}}-1\right)}$ where d_{CC} = 1.42 Å is the stable sp^2 carbon–carbon distance, and d is the interatomic distance of a given carbon atom pair with a cutoff of ~3.2 Å accounting therefore for up to the third nearest neighbors. The sign (±) in this formula is negative only for the second nearest neighbors. This parameterization has been performed by fitting the *ab initio* band structure described in Fig. 1C. The same TB parameterization stands for the 2 × 2 super-cell containing a monomer vacancy defect, meaning that no special treatment is performed for the carbon atoms which are left with a missing neighboring carbon atom which we thus considered to be saturated by hydrogen in the experiment.

Transport methodology

The transport properties are computed from the dynamics of propagating electronic wavepackets with the real-space Kubo–Greenwood method described in detail in ref. 14, 32 and 33. The dynamics is monitored through the time-dependent diffusivity coefficient $D(E, t) = \Delta R^2(E, t)/t$, with E is the energy of the carriers, $\Delta R^2 = \Delta X^2 + \Delta Y^2$, and $\Delta X^2(E,t) = \mathrm{Tr}\left[\delta(E-\hat{H})\left|\hat{X}(t)-\hat{X}(0)\right|^2\right]/\mathrm{Tr}\left[\delta(E-\hat{H})\right]$ the quadratic spreading along the x direction. Tr is the trace over p_z orbitals and $\mathrm{Tr}[\delta(E-\hat{H})]/S = \rho(E)$ is the total DOS (per unit of surface S). The results are averaged over multiple initial random phase wavepackets. The transport properties are inferred from the time evolution of $D(E, t)$. At very short times, the wavepacket dynamics is quasi-ballistic, so that $D(E, t) \propto \nu^2(E)t$, where $\nu(E)$ is the carrier velocity. The dynamics further becomes diffusive as the carriers get scattered by the disorder, and $D(E, t)$ reaches a maximum value $D^{\max}(E) = 2\nu(E)l_e(E)$, where $l_e(E)$ is the mean free path. The semi-classical conductivity then reads $\sigma_{sc}(E) = (1/4)e^2\rho(E)D^{\max}(E)$. All the simulations are conducted at 0 K meaning that the electronic transport is fully coherent. However, it is possible to account for a physical temperature in the evaluation of σ through the use of the Fermi–Dirac distribution. $\sigma_{sc}(E_F,T) = -\frac{1}{4}e^2\int_{-\infty}^{+\infty}\rho(E)D^{\max}(E)\frac{\partial f^{FD}(E,E_F,T)}{\partial E}$. The semi-classical mobility is then defined as $\mu_{sc}(E_F, T) = (\sigma_{sc}(E_F, T))/(en(E_F, T))$ where $n(E_F, T)$ is the charge carrier density. At longer propagation times weak localization corrections due to multiple scattering events per carrier can cause $D(E, t)$ to decrease and possibly vanish on reaching the strong localization regime. To describe the evolution of the conductivity and mobility in the transient regime, either between ballistic and diffusive regimes, or between diffusive or localized regimes, one can define σ and μ at any propagation time or equivalently at any propagation length using $D(E, t)$ instead of $D^{\max}(E)$. The conductivity and the mobility become then extensive quantities which now depend on L computed from the spreading of wave packets as $L = 2\sqrt{\Delta R^2(t,E)}$.

Inverse participation ratio

The inverse participation ratio (IPR) is a measure of the localization of the eigenstates. For a particular eigenstate ψ^α, it is defined as

$$\mathrm{IPR}_\alpha = \frac{\sum_{i=1}^{N_{orb}}|\psi_i^\alpha|^4}{\left|\sum_{i=1}^{N_{orb}}|\psi_i^\alpha|^2\right|^2} \tag{2}$$

where N_{orb} is the number of orbitals. In the present TB model, it is equal to the number of atoms N_{at}. For normalized eigenstates $\left(\sum_{i=1}^{N_{orb}}|\psi_i^\alpha|^2 = 1\right)$ this reduces to $\mathrm{IPR}_\alpha = \sum_{i=1}^{N_{orb}}|\psi_i^\alpha|^4$. This quantity can be integrated over the Brillouin zone to evaluate the energy-dependent IPR. For a wave function localized on a single orbital j, $\psi_i^\alpha = 0$ for $i \neq j$, and hence IPR = 1. For a perfectly delocalized wave function on all orbitals, ψ_i^α has an equal weight on each orbital $\frac{1}{\sqrt{N_{orb}}}$, and hence $\mathrm{IPR} = \frac{1}{N_{orb}}$.

 This journal is © The Royal Society of Chemistry 2016

Acknowledgements

A. L., S. D., A. R. B. M. and J.-C. C. acknowledge financial support from the Fonds de la Recherche Scientifique de Belgique (F. R. S.-FNRS), from the Communauté Wallonie-Bruxelles through the Action de Recherche Concertée (ARC) on Graphene Nano-electromechanics (no. 11/16-037) and from the European ICT FET Flagship entitled "Graphene-based revolutions in ICT and beyond". (no. 604391). J.-J. A. acknowledges support from the Marcel De Merre Prize. Computational resources have been provided by the supercomputing facilities of the Université catholique de Louvain (CISM/UCL) and the Consortium des Equipements de Calcul Intensif en Fédération Wallonie Bruxelles (CECI) funded by the F. R. S.-FNRS.

References

1 K. S. Novoselov, A. K. Geim, S. V. Morozov, D. Jiang, Y. Zhang, S. V. Dubonos, I. V. Grigorieva and A. A. Firsov, *Science*, 2004, **306**, 666.
2 K. S. Novoselov, A. K. Geim, S. V. Morozov, D. Jiang, M. I. Katsnelson, I. V. Grigorieva, S. V. Dubonos and A. A. Firsov, *Nature*, 2005, **438**, 197.
3 K. Kishigi, K. Ueno, E. Miyamoto and Y. Hasegawa, *J. Phys.: Conf. Ser.*, 2011, **334**, 012047.
4 J. Cai, P. Ruffieux, R. Jaafar, M. Bieri, T. Braun, S. Blankenburg, M. Muoth, A. Seitsonen, M. Saleh, X. Feng, K. Müllen and R. Fasel, *Nature*, 2010, **466**, 470–473.
5 J.-J. Adjizian, P. Briddon, B. Humbert, J.-L. Duvail, P. Wagner, C. Adda and C. Ewels, *Nat. Commun.*, 2014, **5**, 5842.
6 A. P. Côté, A. I. Benin, N. W. Ockwig, M. O'Keeffe, A. J. Matzger and O. M. Yaghi, *Science*, 2005, **310**, 1166–1170.
7 J. Feldblyum, C. McCreery, S. Andrews, T. Kurosawa, E. Santos, V. Duong, L. Fang, A. Ayzner and Z. Bao, *Chem. Commun.*, 2015, **51**, 13894.
8 Z. Xiang and D. Cao, *Macromol. Rapid Commun.*, 2012, **33**, 1184.
9 Z. Xiang, D. Cao, L. Huang, J. Shui, M. Wang and L. Dai, *Adv. Mater.*, 2014, **26**, 3315.
10 J. Mendoza-Cortes, S. Han, H. Furukawa, O. Yaghi and W. A. Goddard, *J. Phys. Chem. A*, 2010, **114**, 10824–10833.
11 S. Wan, J. Guo, J. Kim, H. Ihee and D. Jiang, *Angew. Chem., Int. Ed.*, 2008, **47**, 8826–8830.
12 V. Pereira, J. L. dos Santos and A. Castro-Neto, *Phys. Rev. B: Condens. Matter Mater. Phys.*, 2008, **77**, 115109.
13 O. V. Yazyev and S. Louie, *Nat. Mater.*, 2010, **9**, 806.
14 A. Lherbier, S. Dubois, X. Declerck, Y.-M. Niquet, S. Roche and J.-C. Charlier, *Phys. Rev. B: Condens. Matter Mater. Phys.*, 2012, **86**, 075402.
15 A. Cresti, F. Ortmann, T. Louvet, D. V. Tuan and S. Roche, *Phys. Rev. Lett.*, 2013, **110**, 196601.
16 P. A. Lee and T. V. Ramakrishnan, *Rev. Mod. Phys.*, 1985, **57**, 287–337.
17 J. M. Soler, E. Artacho, J. D. Gale, A. Garca, J. Junquera, P. Ordejon and D. Sanchez-Portal, *J. Phys.: Condens. Matter*, 2002, **14**, 2745.
18 E. Artacho, E. Anglada, O. Dieguez, J. D. Gale, A. Garca, J. Junquera, R. M. Martin, P. Ordejon, J. M. Pruneda, D. Sanchez-Portal and J. M. Soler, *J. Phys.: Condens. Matter*, 2008, **20**, 064208.
19 A. Botello-Méndez, A. Lherbier and J.-C. Charlier, *Solid State Commun.*, 2013, **175–176**, 90–100.
20 A. Lherbier, A. Botello-Méndez and J.-C. Charlier, *Nano Lett.*, 2013, **13**, 1446.
21 P. W. Brouwer, E. Racine, A. Furusaki, Y. Hatsugai, Y. Morita and C. Mudry, *Phys. Rev. B: Condens. Matter Mater. Phys.*, 2002, **66**, 014204.
22 A. H. Castro-Neto, F. Guinea, N. M. R. Peres, K. S. Novoselov and A. K. Geim, *Rev. Mod. Phys.*, 2009, **81**, 109–162.
23 I. Meric, M. Han, A. Young, B. Ozyilmaz, P. Kim and K. Shepard, *Nat. Nanotechnol.*, 2008, **3**, 654.
24 R. Haydock, *Comput. Phys. Commun.*, 1980, **20**, 11–16.
25 S. Das Sarma, S. He and X. C. Xie, *Phys. Rev. Lett.*, 1988, **61**, 2144–2147.
26 G. G. Naumis, *Phys. Rev. B: Condens. Matter Mater. Phys.*, 2007, **76**, 153403.
27 N. Leconte, J. Moser, P. Ordejón, H. Tao, A. Lherbier, A. Bachtold, F. Alsina, C. S. Torres, J.-C. Charlier and S. Roche, *ACS Nano*, 2010, **4**, 4033–4038.
28 Y. V. Skrypnyk and V. M. Loktev, *Phys. Rev. B: Condens. Matter Mater. Phys.*, 2011, **83**, 085421.
29 J. P. Perdew, K. Burke and M. Ernzerhof, *Phys. Rev. Lett.*, 1996, **77**, 3865.
30 N. Troullier and J. L. Martins, *Phys. Rev. B: Condens. Matter Mater. Phys.*, 1991, **43**, 1993.
31 H. Monkhorst and J. Pack, *Phys. Rev. B: Solid State*, 1976, **13**, 5188.
32 S. Roche and D. Mayou, *Phys. Rev. Lett.*, 1997, **79**, 2518.
33 N. Leconte, A. Lherbier, F. Varchon, P. Ordejón, S. Roche and J.-C. Charlier, *Phys. Rev. B: Condens. Matter Mater. Phys.*, 2011, **84**, 235420.

This journal is © The Royal Society of Chemistry 2016